Pergamon

Int. J. Heat Mass Transfer. Vol. 40, No. 16, pp. 3837–3847, 1997

Printed in Great Britain
0017–9310/97 $17.00+0.00

PII: S0017–9310(97)00011–2

Solidification of ternary metal alloys—II. Predictions of convective phenomena and solidification behavior in Pb–Sb–Sn alloys

MATTHEW JOHN M. KRANE† and FRANK P. INCROPERA

Heat Transfer Laboratory, School of Mechanical Engineering, Purdue University, West Lafayette, IN 47907, U.S.A.

(*Received* 9 *February* 1996 *and in final form* 20 *December* 1996)

Abstract—In Part I of this work, the continuum mixture model for binary alloys was extended to three component systems and used an idealized ternary phase diagram to provide the supplemental thermodynamic relations needed to close the model. In this paper, the new model is applied to the solidification of four lead-rich Pb–Sb–Sn alloys. System-specific information needed to close the model presented in Part I is extracted from the lead–antimony–tin phase diagram. Numerical simulations are performed to demonstrate similarities and differences between the macrosegregation patterns and convective flows of these ternary alloys and of two component systems. Macrosegregation of the solutes is altered significantly from the familiar patterns of the binary systems only when solidification in the doubly saturated binary troughs occurs near the liquidus interface. If the secondary and tertiary crystallization occur deep in the mushy zone, the resulting microsegregation has only small effects on the final redistribution of solute.

1. INTRODUCTION

In a companion paper, Krane *et al.* [1], have extended the binary continuum mixture equations [2, 3] to include a third component and used a generic ternary equilibrium phase diagram to derive supplemental thermodynamic relations to close the model. In addition to primary solidification, this model accounts for the possibility of secondary and tertiary crystallization in binary eutectic troughs and at ternary eutectic and peritectic points. The present paper examines the application of this new model to the lead-rich corner of the Pb–Sb–Sn system. The three component phase diagram is idealized for convenient extraction of the information required by the closure rules [1]. Calculations are performed for four different alloy compositions, all with lead as the primary precipitant, and the numerical results are compared with flow and macrosegregation patterns previously computed for binary alloys.

2. PHASE DIAGRAM AND THERMODYNAMIC CLOSURE MODEL

The generalized phase diagram in ref. [1] was constructed to include regions of primary crystallization, binary eutectic valleys (troughs) and two types of ternary invariant points, all of which are features from which the thermodynamic model can be used to extract the temperature and the phase fractions and compositions. These features, which are found in many three component systems, particularly in aluminum-rich ternary alloys, also characterize the Pb–Sb–Sn system shown in Fig. 1. One reason for using this system is that, depending on the initial composition, lead-rich alloys, defined by the region [Pb–e_{Pb-Sb}–e_{Pb-Sn}], of this relatively simple three component system may have liquid composition paths which pass through any of the foregoing features. Other advantages include a well defined phase diagram and low liquidus temperatures, facilitating experimental verification of the predicted temperature histories and final composition profiles.

The lead-rich corner of Fig. 1. is bordered by the Pb–Sb and Pb–Sn binary phase diagrams, both of which are simple eutectic systems. The Pb–Sb system has a eutectic point (e_{Pb-Sb}) at 251°C and 11.2 wt%Sb. The maximum solid solubility of antimony in the Pb-rich α solid is 3.5 wt%Sb. The Pb–Sn system also contains a eutectic ($T_{EUT} = 183°C, f^{Sn}_{EUT} = 0.619$), while the maximum solutiblity of Sn in the α solid is 19.2 wt%. The two diagrams intersect at pure Pb, which has a melting point at 327°C.

The ternary Pb–Sb–Sn diagram is divided into two sections by the pseudobinary Pb–SbSn system, where SbSn is an intermetallic compound. The Pb–SbSn system has a eutectic point ($e_{Pb-SbSn}$) at 10 wt%Sb–10 wt%Sn and 245°C. The partial system Pb–Sb–SbSn has a ternary eutectic point (E) at 12 wt%Sb–4 wt%Sn and 240°C. This invariant point is found at the intersections of the binary troughs which represent the α–

†Present address: School of Materials Engineering, Purdue University, West Lafayette, IN 47907, U.S.A.

NOMENCLATURE

f	mass fraction	κ_o	permeability constant.
g	volume fraction		
k	equilibrium partition coefficient		
K	permeability [m^2]		
M^A	overall macrosegregation of element A		
t	time [s]	Subscripts	
T	temperature [K]	BIN	binary trough
U	overall heat transfer coefficient [W m^{-2} K^{-1}]	c	sink temperature
		EUT	eutectic point
V	volume [m^3]	l	liquid
x, y	Cartesian coordinates [m].	LIQ	liquidus
		o	initial
Greek symbols		s	solid
$\alpha, \beta, \gamma, \delta$	primary solid phases	SOL	solidus.

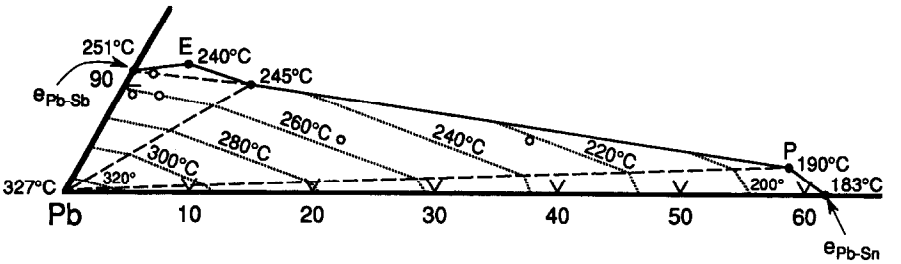

Fig. 1. Linearized liquidus surface of lead rich-corner of Pb–Sb–Sn system. Open circles indicate initial compositions of simulations found in Table 3.

β, α–δ and β–δ eutectic separations, where δ is the Sb-rich and β is the SbSn-rich primary solid phase. The partial system Pb–Sn–SbSn, also has an invariant point, a ternary peritectic (P) at 190°C and 2.5 wt%Sb–57.5 wt%Sn. Two monovariant curves, the α–β and the β–γ binary troughs (where γ is the primary Sn-rich solid), intersect at P, and the binary valley for the α–γ runs down from P to $e_{Pb\text{–}Sn}$ at 183°C.

In order to close the continuum mixture model [1] for the solidification of lead-rich Pb–Sb–Sn alloys, certain information must be extracted from the phase diagram and related data presented by Osamura [4]. Specifically, the supplemental thermodynamic relations in reference [1] require the location of the invariant points (described above), the paths of the binary troughs, the values of the equilibrium partition coefficients and the location of the liquidus surface.

The paths of the four binary troughs which bound the region of primary α crystallization are linearized between the five invariant points ($e_{Pb\text{–}Sb}$, E, $e_{Pb\text{–}SbSn}$, P, $e_{Pb\text{–}Sn}$). These paths are written in terms of liquid composition and temperature,

$$f_l^{Sb} = A_{Sb}T + B_{Sb} \quad (1)$$

$$f_l^{Sn} = A_{Sn}T + B_{Sn} \quad (2)$$

where the constants in equations (1) and (2) are provided in Table 1.

The equilibrium partition coefficients for the phase i and element j are defined as

$$k_i^j = f_i^j / f_l^j. \quad (3)$$

The values of this coefficient for the primary α solidification are equated to those for the two binary systems which bound the Pb-rich corner. The liquid compositions at which the β, γ and δ solid phases form are all in the binary troughs, which correspond to solid β, γ and δ compositions estimated from several isothermal sections of the ternary diagram in ref. [4]. The resulting equilibrium partition ratios for these phases are written as functions of temperature and are found in Table 2.

The liquidus surface in the primary α crystallization region is also simplified for ease of calculation. The surface is divided into four triangular planes (indicated by the dashed lines in Fig. 1), using the invariant points as vertices. The temperatures on the sides of the triangles are linear interpolations between the end points. Connecting these points across the faces of these triangles gives the temperatures on the linearized liquidus surface.

Table 1. Phase diagram data. Coefficients for binary trough paths in equations (1) and (2)

Range	A_{Sb} (wt%/°C)	B_{Sb} (wt%)	A_{Sn} (wt%/°C)	B_{Sn} (wt%)
$0 < f_l^{Sn} < 0.04$	−0.0007143	0.2914	−0.003571	0.8971
$0.04 < f_l^{Sn} < 0.1$	−0.0040	1.080	0.0120	−2.84
$0.1 < f_l^{Sn} < 0.575$	0.001364	−0.2341	−0.008636	2.2159
$0.575 < f_l^{Sn} < 0.619$	0.003571	−0.6536	−0.006286	1.7693

Table 2. Phase diagram data. Functions for equilibrium partition coefficients k_l^i ($i = \alpha, \delta, \beta, \gamma$; j = Sb, Sn). Temperatures are in °C

	Sb	Sn
α (Pb)	0.310	0.304
δ (Sb)	$[(0.003571)T+0.06286] \times [(-0.0007143)T+0.2914]^{-1}$	$[(0.004464)T+1.1214] \times [(-003571)T+0.8971]^{-1}$
β (SbSn) for $f_l^{Sn} < 0.1$	$[(-0.0240)T+6.34] \times [(-0.0040)T+1.080]^{-1}$	$[(0.0340)T-7.87] \times [(0.0120)T+2.84]^{-1}$
β (SbSn) $f_l^{Sn} > 0.1$	$[0.46] \times [0.001364)T-0.2341]^{-1}$	$[(-0.0007273)T+0.6382] \times [(-0.008636)T+2.2159]^{-1}$
γ (Sn)	$[(0.01286)T-2.3529] \times [(0.003571)T-0.6356]^{-1}$	$[(-0.01357)T+3.4586] \times [(-0.006286)T+1.7693]^{-1}$

3. MATHEMATICAL FORMULATION AND NUMERICAL METHODS

Simulation of the solidification of three component alloys is performed in a two dimensional, 100 mm square domain. The ingot is presumed to be cooled by a convection condition at the left wall while the other three sides are insulated. A representative value of the overall heat transfer coefficient, $U = 100$ W m^{-2} K^{-1}, which accounts for mold wall conduction, as well as convection, is used for all of the simulations. All four walls are treated with a no-slip condition and are impermeable to mass and species transport.

The transport equations for mixture mass, momentum, energy and species, which assume negligible solid motion and shrinkage effects, are presented in the companion paper [1]. A simple Blake–Cozeny expression is used to calculate the permeability function, K, for the mushy zone, which is assumed to be isotropic

$$K = \kappa_0 \frac{g_l^3}{(1-g_l)^2}. \tag{4}$$

A permeability constant of $\kappa_0 = 5 \times 10^{-10}$ m^2 is calculated from dendritic arm spacing data found in Sarazin and Hellawell [5]. The phase fractions and compositions and the temperature needed to close the transport equations are found by combining the data of Tables 1 and 2 and Fig. 1 with the thermodynamic closure model of Krane *et al.* [1].

The numerical scheme used to solve the conservation equations (the SIMPLER algorithm) is a control-volume-based finite difference method, with a fully implicit time marching technique [6]. The program uses a TDMA line-by-line solver with a block correction method, solving first for the pressure and velocity fields and then for the mixture enthalpy and composition. The grid (85 × 125) provides a compromise between computational accuracy and speed and is comparable to that used in previous simulations of lead–tin systems [7]. The largest time steps which yielded quickly converged results increased during solidification, as the cooling rate decreased with increasing global solid fraction. For most cases, the initial time step was 0.25 s and was increased sequentially to 2 s near the end of solidification. Solutions were considered converged at a time step if they had residuals of mass, energy and species less than 0.0001 for at least five consecutive iterations. The calculations were performed on an HP-715 workstation cluster.

4. NUMERICAL RESULTS AND DISCUSSION

In order to study possible solidification behaviors of ternary metal alloys, four numerical simulations were performed, each with a different initial composition from the lead-rich corner of the phase diagram. These compositions are noted on Fig. 1 as open circles, and the exact values are given in Table 3. This table also includes the liquidus and solidus temperatures, the mass fraction solid at the end of primary crystallization, the time for complete freezing and the macrosegregation levels found in the final cast, for each of the four cases. The last datum, M^A, is an average redistribution of component A (Sn or Sb), integrated over the ingot

$$M^A = \left[\frac{1}{V}\int_V (f_m^A - f_o^A)^2 \, dV\right]^{1/2}. \tag{5}$$

The initial temperatures were 20°C higher than the liquidus temperature for all cases and $T_c = 12$°C.

Table 3. Initial compositions, phase diagram data and results for four simulations

	f^{Sn}	f^{Sb}	T_{LIQ} (°C)	T_{SOL} (°C)	$f_{s,BIN}$	t_{SOL} (s)	M^{Sn}	M^{Sb}	M^{Sn}/f_o^{Sn}	M^{Sb}/f_o^{Sb}
Case 1	0.03	0.09	262	240	0.36	2466	0.0218	0.0073	0.243	0.243
Case 2	0.01	0.09	265	243	0.31	2397	0.0191	0.0026	0.212	0.258
Case 3	0.015	0.11	250	241	0.07	2415	0.0060	0.0145	0.055	0.145
Case 4	0.35	0.05	222	190	0.13	3211	0.0131	0.111	0.261	0.381

For Case 1 ($f_o^{Sn} = 0.03$ and $f_o^{Sb} = 0.09$) solidification begins with the liquid composition moving along the liquidus surface towards the ternary eutectic point, E. As solidification proceeds, the liquid composition path only traverses the primary surface and ends at E, with little or no time spent in either of the binary troughs, which end at that invariant point. Therefore, it is expected that the macrosegregation patterns and convective flows should be similar to those found in a solidifying binary system [7].

Figure 2 shows the redistribution of tin and antimony and the streamlines at $t = 250$ s for Case 1. The streamlines show two major convective cells. The counterclockwise thermal cell, caused by the removal of heat from the melt into the colder mushy zone, occupies roughly half of the liquid region. In the mushy zone, tin and antimony are rejected into the liquid as freezing proceeds, causing a positive buoyancy force which drives the interdentritic liquid up and out into the melt. This flow is seen in the clockwise cell along the top 40% of the liquidus interface in Fig. 2. The rejected solutes are seen forming a light, Sn- and Sb-rich layer along the cavity top. A negatively segregated cone forms at the bottom of the mushy zone, as the rising solute-rich liquid is replaced by liquid from the melt which is closer to the initial composition. Also, A-segregates (or, channels) have begun to form. These locations have relatively low solid volume fractions due to the lower liquidus temperature associated with the mixture composition. Hence, they provide preferred flow paths for interdentritic fluid. In this first case, the liquid in the channels is rich in tin and antimony and rises through the A-segregates into the melt.

In Fig. 3, the final macrosegregation plots show the well-known patterns for binary eutectic alloys. There is a negatively segregated cone on the bottom of the cavity next to the chill wall and a positive cone segregate along the top and far walls. A-segregates, larger than in Fig. 2, are seen stretching up and away from the chilled surface. These patterns are similar to those of binary alloys because the solidification path indicates only primary α and eutectic freezing, as one would find in Pb–Sn or Pb–Sb alloys. It should be noted that the normalized macrosegregation levels (M^A/f_o^A) for the two solutes is approximately the same. As noted by Schneider and Beckermann [8], the global macrosegregation levels of various solutes with only primary solidification are linearly dependent on the equilibrium partition coefficients of those solutes. As seen in Table 2, $k_\alpha^{Sn} \approx k_\alpha^{Sn}$, so the redistribution of the tin and antimony should be roughly the same.

For Cases 2 and 3, initial compositions were selected so that the solidification paths would travel along the binary trough [e_{Pb-Sb}–E] for significant portions of the freezing processes, but would completely solidify before the ternary eutectic point was reached. Case 2 had $f_o^{Sn} = 0.01$ and $f_o^{Sb} = 0.09$, while Case 3 had $f_o^{Sn} = 0.015$ and $f_o^{Sb} = 0.11$. The significant difference between these two compositions is the distribution of the solidification paths between primary α crystallization and the twofold saturation curve. Case 2 has a mass fraction solid of approximately 0.31 when the path of liquid composition intersects the binary trough. The fraction solid at this transition point (the beginning of precipitation of Sb-rich solid) for Case 3 is 0.07, which means that almost all of the liquid composition path for this alloy is along the [e_{Pb-Sb}–E] valley.

The basic development of the flow patterns, solidification fronts and solute redistributions occur in ways similar to Case 1. Tin and antimony are rejected throughout the freezing process and the resulting lighter liquid rises and leaves the mushy zone, creating positive and negative cone segregates with some channelling. However, there are important differences between Cases 2 and 3. The final solute distribution in Case 2 shows a pattern remarkably similar to that of a binary alloy, with approximately the same normalized levels of macrosegregation as Case 1. Cases 1 and 2 ended primary crystallization at $f_s \approx 0.36$ and $f_s \approx 0.30$, respectively. As suggested by the mushy zone scaling analysis of Krane and Incropera [9], fluid flow which has a significant effect on solute redistribution in the time frame of complete solidification does not occur very deep in the mushy zone. Most of the noticeable Sn and Sb transport occurs in regions with solid mass fraction much lower than 0.3. Therefore, in Case 2, most of the macrosegregation pattern is established before the binary precipitation of α and δ begins. The composition in Case 3, however, was chosen so that some α–δ solidification would occur in regions close to the liquidus interface, where there was significant advection of solute. This qualitative change in solidification path results in a significant quantitative change in the overall macrosegregation levels. In Case 3, M^{Sb}/f_o^{Sb} is significantly lower than in Case 2 (see Table 3) because, on the binary trough [e_{Pb-Sb}–E], the antimony composition of the liquid is almost constant and very close to the initial value. This small

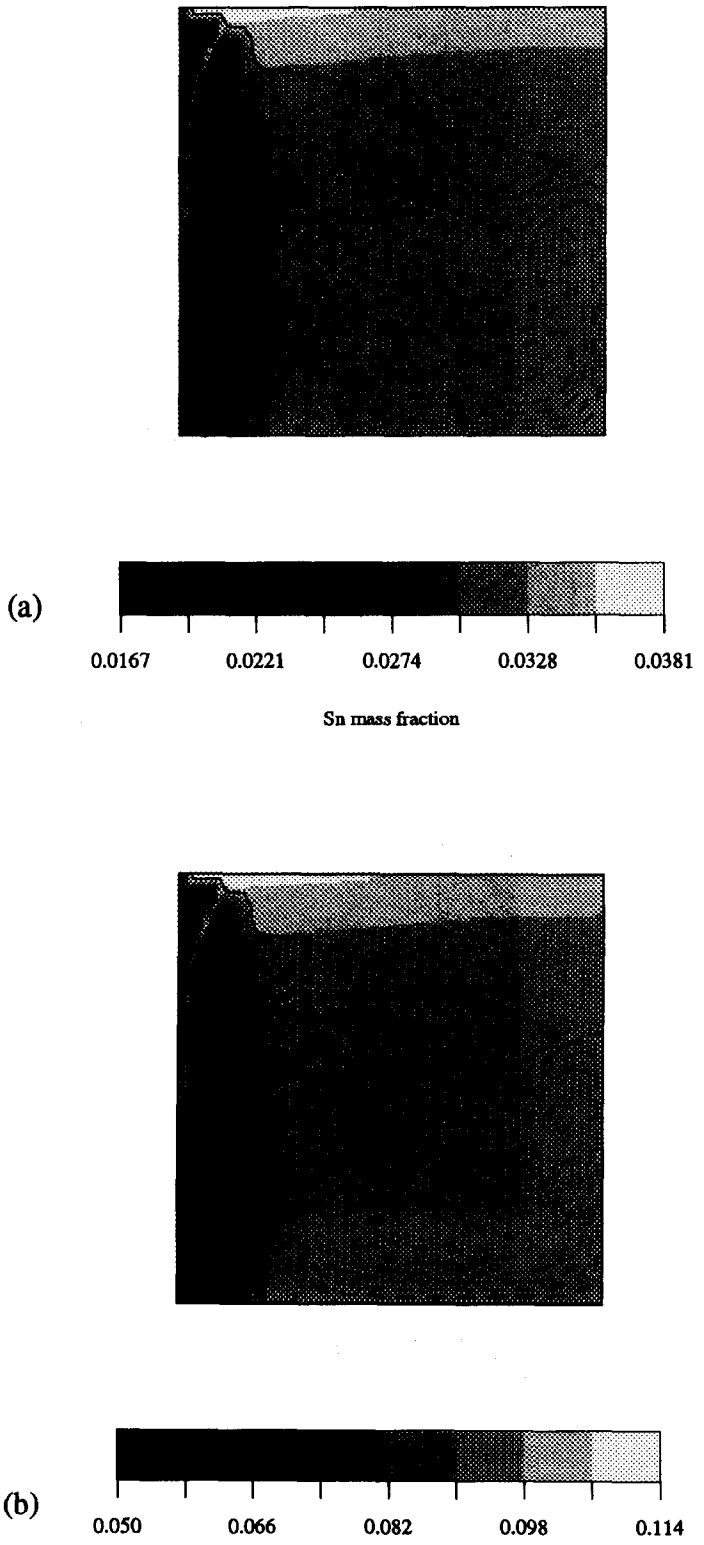

Fig. 2. Case 1 at 250 s: (a) f^{Sn}; (b) f^{Sb} (solid = CW cell, dashed = CCW cell).

change in the f_l^{Sb} results in much less global and local segregation of antimony, but also a lower value of M^{Sn}/f_o^{Sn}. Because the Sb content of the liquid is much more uniform in Case 3, the antimony contributes much less to the solutal buoyancy force, resulting in weaker flows. Even though there is significant local

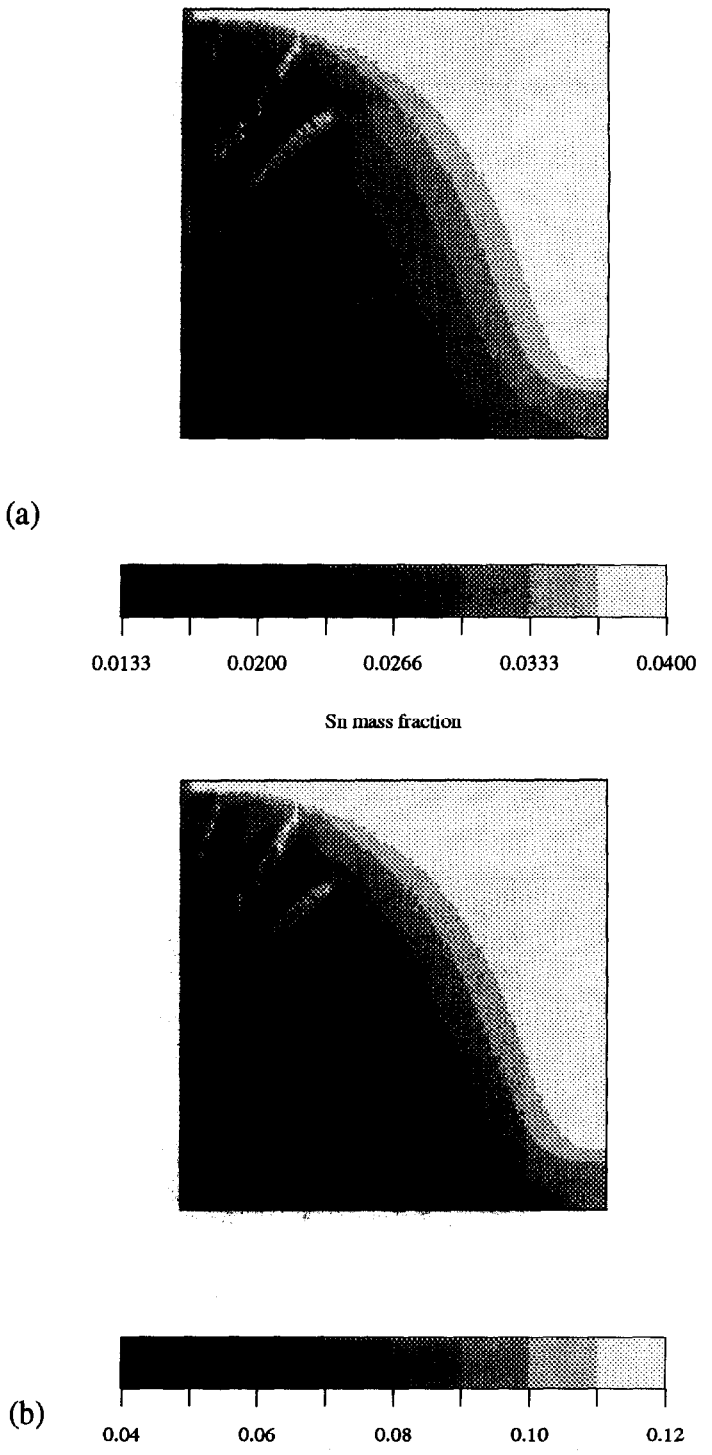

Fig. 3. Case 1 after complete solidification: (a) f^{Sn}; (b) f^{Sb}.

segregation of tin between the solid and the liquid, the less vigorous flows do not advect this tin-rich fluid at as fast a rate as in Case 2.

The last composition takes a different type of path from those previously discussed. Case 4 begins with primary α crystallization, but soon its liquid compositions falls into the binary trough [$e_{Pb\text{-}SbSn}$–P], which is twofold saturation curve for α and the SbSn-rich β solid phase, and ends its solidification at the peritectic point, P. Because the solidification path for the initial composition of Case 4 ($f_o^{Sn} = 0.35$, $f_o^{Sb} = 0.05$) intersects the binary trough at $f_s \approx 0.13$,

one should expect the trough to affect flow development and solute redistribution. It is important to note that, while the tin content of the liquid along the entire solidification path increases monotonically, the liquid concentration of antimony only increases during primary freezing. After the liquid composition has reached the binary trough, the antimony concentration in the liquid falls to half of its initial value. The slope of this binary trough results in opposite Sn and Sb segregation, similar to the Al and $NiAl_3$ partition described in Mehrabian and Flemings [10]. However, in this case, the final distribution is different from ref. [10] because segregation in that study was controlled by shrinkage induced flow only, rather than the buoyancy induced flow in the present paper.

Before freezing begins in the binary trough, the macrosegregation patterns are similar to those of Fig. 2 which is to be expected, as only primary solidification has occurred by this time. The effect of the decreasing liquid composition along the binary trough begins to be apparent in Fig. 4 which corresponds to $t = 500$ s. While the Sn distribution has proceeded as in previous cases, the Sb plot reveals some differences, as the local liquid concentrations of antimony in regions of binary solidification began to decrease. Along the top of the cavity a region of Sb-depleted liquid has begun to form. Figure 4 shows a clockwise circulation pattern which is wholly dominated by solutally driven flow. Although the depletion of antimony from the liquid causes a downward buoyancy force, the large tin enrichment of the same liquid is more than enough to create a net force which is strongly positive.

To demonstrate the local redistribution of solute which leads to the expulsion of Sn-rich and Sb-poor liquid, Fig. 5 includes enlarged views of the upper corner of the cavity near the chill wall. A solid line of $f_s = 0.5$ is superimposed on the tin and antimony distributions to highlight the location of the channels. In Fig. 5(a), the tin content below each channel is lower than the nominal composition. As solidification proceeded, the regions below the A-segregates rejected tin into the liquid. This liquid rose into the channels, which provided preferred flow paths due to their relatively high permeability. The Sn-rich liquid then travelled up the channel, emerging near the top of the melt. At the same time that large changes in tin content of the liquid were driving the liquid up and out of the mushy zone through the A-segregates, the regions below the channels had reached mixture compositions and temperatures with liquid compositions corresponding to the binary trough. Therefore, while tin was rejected from the forming solid, the solidification process was depleting the Sb content of the liquid, as shown by the Sb-rich regions below the channels in Fig. 5(b). The A-segregates themselves are Sb-poor, as the antimony depleted liquid was carried into the channels by the Sn dominated flow. This process continued until the solidification fronts advanced, the local permeability in the channels decreased, and a tin enriched, antimony depleted region was left behind as fluid flow became negligible.

The final Sn and Sb plots for this case are seen in Fig. 6. Although the Sn macrosegregation in Fig. 6(a) shows the same pattern seen in previous cases and in binary systems, the redistribution of Sb in Fig. 6(b) is quite different. While the initial primary solidification occurred over a long enough time to create a small negatively segregated cone in the lower left corner and to begin channel formation, as freezing continued, the mush began to reject Sb-poor liquid, which, buoyed by the large increase in Sn content, remained near the top of the cavity to form a negative segregate along the top and right walls of the ingot.

5. SUMMARY

In a companion paper [1], the continuum mixture model for two component alloy solidification [2, 3] was modified to include a third component. A generic ternary phase diagram was used to derive the thermodynamic closure model required by the transport equations for mixture mass, momentum, enthalpy and species. In this study, the new model is applied to the lead-rich corner of the Pb–Sb–Sn system. The actual equilibrium phase diagram for these three elements is linearized, and this idealization is used to obtain data necessary for the thermodynamic model proposed in [1]. Numerical simulations of solidification of four different alloys in a square mold are performed, and the flow and solute redistribution patterns are examined.

The first alloy (case 1) has an initial composition which has a solidification path along the liquidus surface and includes only primary and eutectic solidification. Because this type of path is found in two component alloys, the development of the convective flow and consequent solute mass fraction fields resemble those for a binary system. Two other alloys (cases 2 and 3) are examined in which there was significant solid formation in the binary trough from which the primary lead and antimony solid phases precipitate. The first of these two cases shows little effect of freezing along that binary valley. Here, the liquid composition is only on that curve in regions of the mushy zone which have high solid fractions (low permeabilities) and negligible fluid flow. In spite of the microsegregation caused by the twofold saturation line, on a macroscopic scale, the weak fluid flow does not have time to move the liquid a significant distance before freezing is complete. The second of these two systems (case 3) has almost no change in liquid composition of antimony because of its solidification path. This causes a severe reduction of Sb redistribution compared to case 2 and weakens the buoyancy induced flow due to the much reduced contribution of antimony to the buoyancy force.

The final alloy (case 4) also begins solidification in the primary crystallization region, but has significant freezing on the twofold saturation curve for the pri-

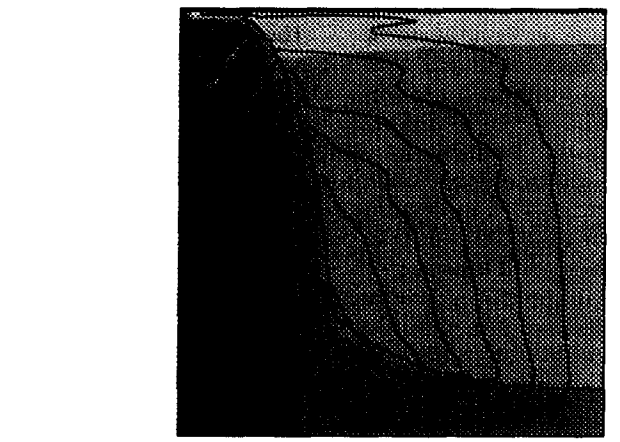

(a)

Sn mass fraction

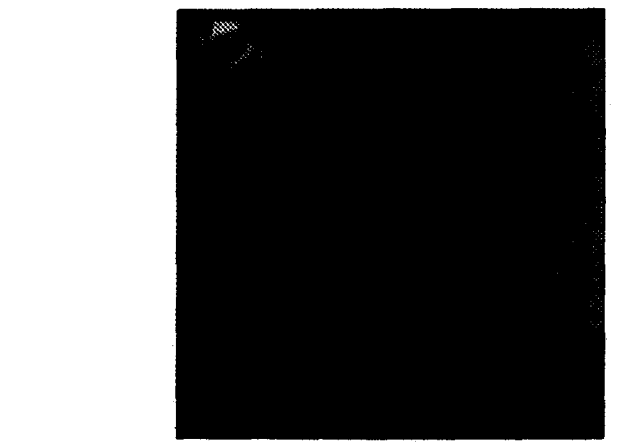

(b)

Sb mass fraction

Fig. 4. Case 4 at 500 s: (a) f^{Sn}; (b) f^{Sb} (CW cell).

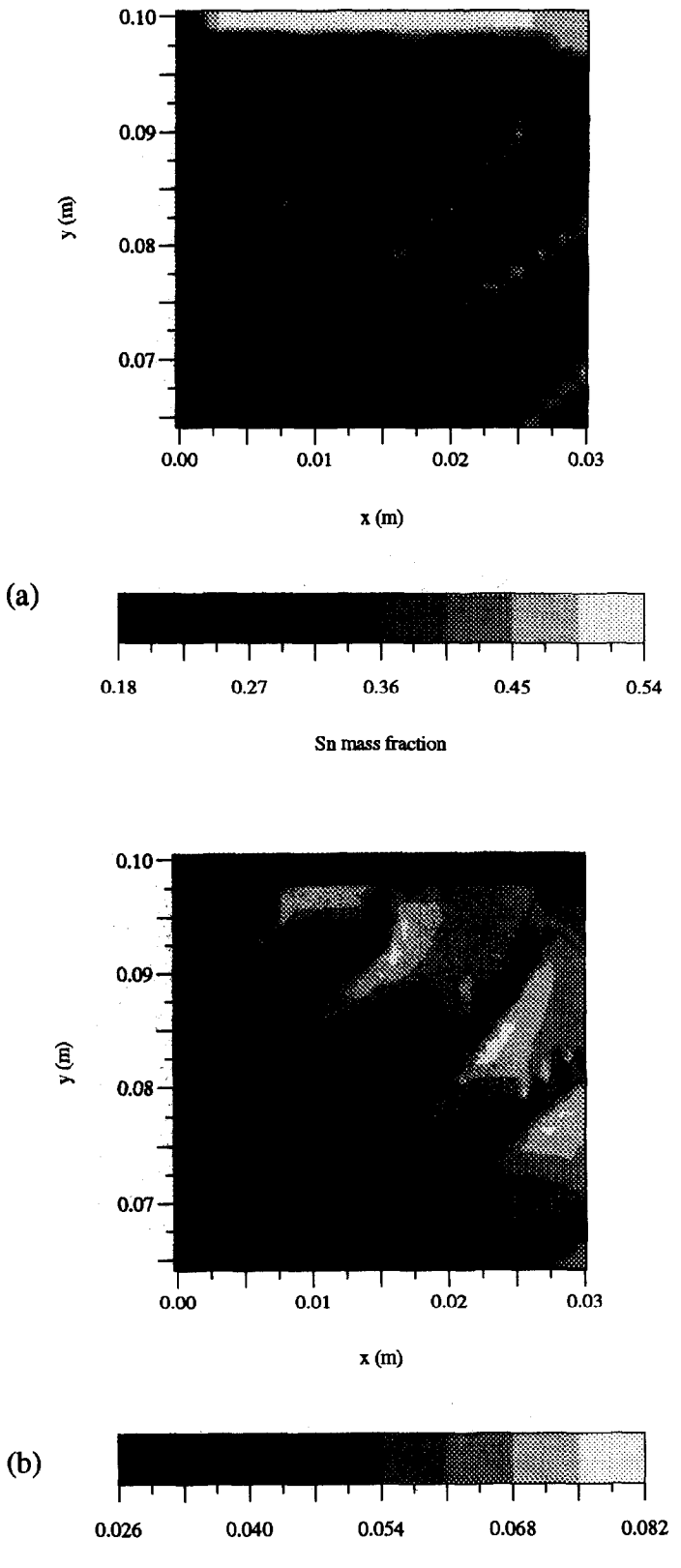

Fig. 5. Detail of upper left corner of Case 4 at 1000 s: (a) f^{Sn}; (b) f^{Sb}.

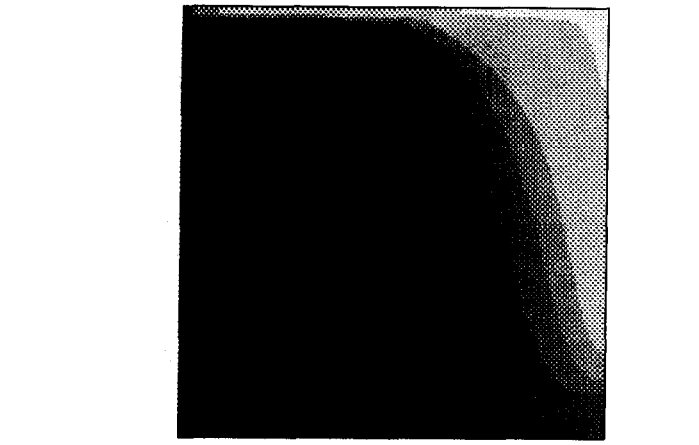

(a)

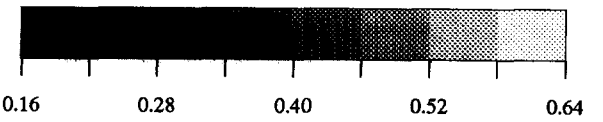

(b)

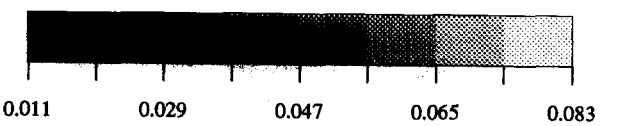

Fig. 6. Case 4 after complete solidification: (a) f^{Sn}; (b) f^{Sb}.

mary Pb and SbSn solid phase (α and β, respectively). In this case, the tin content of the liquid increases with lower temperatures, while the liquid antimony concentration first increases (in the primary region) and then falls (along the binary trough). This reversal of Sb *micro*segregation leads to a unique pattern of antimony *macro*segregation. The convective flows, dominated by the large difference in Sn content of the interdendritic fluid and the bulk melt, begin to redistribute the antimony as in a two component alloy. Once the binary trough is reached, however, the newly formed solid absorbs, rather than rejects, the antimony, and liquid advected from the mush by the Sn-driven flows is Sb-poor. The resulting pattern, with negative antimony cone segregates in the lower left and upper right corners, separated by a region of Sb-rich material, is unique to some ternary alloys and is not found in two component systems or in multicomponent alloys which only experience primary solidification.

Acknowledgements—The authors would like to thank the Department of Energy for support of this research through Award Number DE-FG02-87 ER13759.

REFERENCES

1. Krane, M. J. M. and Incropera, F. P., Solidification of ternary metal alloys—I. Model development. *International Journal of Heat and Mass Transfer*, 1997, **40,** 3827–3835.
2. Bennon, W. D. and Incropera, F. P., A continuum model for momentum, heat and species transport in binary solid–liquid phase change systems—I. model formulation. *International Journal of Heat and Mass Transfer*, 1987, **30,** 2161–2170.
3. Prescott, P. J., Incropera, F. P. and Bennon, W. D., Modelling of dendritic solidification systems: reassessment of the continuum momentum equation. *International Journal of Heat and Mass Transfer*, 1991, **34,** 2351–2359.
4. Osamura, K., The Pb–Sb–Sn (lead–antimony–tin) system. *Bulletin of Alloy Phase Diagrams*, 1985, **6,** 372–379.
5. Sarazin, J. R. and Hellawell, A., Channel formation in Pb–Sn, Pb–Sb and Pb–Sn–Sb alloy ingots and comparison with the system NH_4Cl–H_2O. *Metallurgical Transactions*, 1988, **19A,** 1861–1871.
6. Patankar, S., *Numerical Heat Transfer and Fluid Flow*. Hemisphere, New York, 1980.
7. Prescott, P. J. and Incropera, F. P., Convective transport phenomena and macrosegregation during solidification of a binary metal alloy: I—numerical predictions. *Journal of Heat Transfer*, 1994, **116,** 735–741.
8. Schneider, M. C. and Beckermann, C., Formation of macrosegregation by multicomponent thermosolutal convection during solidification of steel. *Metallurgical and Materials Transactions*, 1995, **26A**, 2373–2388.
9. Krane, M. J. M. and Incropera, F. P., A scaling analysis of the unidirectional solidification of a binary alloy. *International Journal of Heat and Mass Transfer*, 1996, **39,** 3567–3579.
10. Mehrabian, R. and Flemings, M. C., Macrosegregation in ternary alloys. *Metallurgical Transactions*, 1970, **1,** 455–464.